Supplementary Information

for

Electron Spin Resonance of Single Molecules and Magnetic Interaction through Ligands

Xue Zhang[1,2], Christoph Wolf[1,2], Yu Wang[1,2], Hervé Aubin[3], Tobias Bilgeri[4], Philip Willke[1,2,5], Andreas J. Heinrich[1,6]* and Taeyoung Choi[1,6]*

1 Center for Quantum Nanoscience, Institute for Basic Science (IBS), Seoul 03760, Republic of Korea

2 Ewha Womans University, Seoul 03760, Republic of Korea

3 Universités Paris-Saclay, CNRS, Centre de Nanosciences et de Nanotechnologies, 91120, Palaiseau, France

4 Institute of Physics, École Polytechnique Fédérale de Lausanne, Station 3, CH-1015 Lausanne, Switzerland

5 Karlsruhe Institute of Technology, Karlsruhe 76131, Germany

6 Department of Physics, Ewha Womans University, Seoul 03760, Republic of Korea

1. Kondo splitting in varied external magnetic fields

Individual FePc molecule shows zero-bias peak in dI/dV spectrum measured by a non-magnetic tip at zero field, which is the signature of Kondo resonance (Fig. S1(a)-(b)). By applying a magnetic field, the zero-bias peak splits into two excitation steps, corresponding to an inelastic excitation between the spin states with quantum number $m_s = +1/2$ and $m_s = -1/2$. The splitting indicates the Zeeman energy of the FePc spin, $E_{\mathrm{Zeeman}} = g\mu_{\mathrm{B}}B_{\mathrm{ex}}$ (μ_{B} is the Bohr magneton, B_{ex} is the magnetic field). The zero-bias peak splits in a similar way when the external field is along in-plane (B_{x}) and out-of-plane (B_{z}) direction. By fitting our dI/dV spectra with the scattering model proposed by Markus Ternes[40,41], we obtained the g-factors of 2.42 and 2.35 in B_{x} and B_{z}, respectively. The comparable g-factors in both in-plane and out-of-plane direction reveal that FePc spin is lack of magnetic anisotropy and can be treated as a free electron spin, as confirmed by our ESR measurements (Supplementary Section 2 and 3). Notably, the Kondo resonance can only be detected at molecule central area while the lobes are spectroscopically featureless. Figure S1(c) displays the dI/dV measured on an individual FePc with a spin-polarized tip, showing the asymmetry around zero bias.

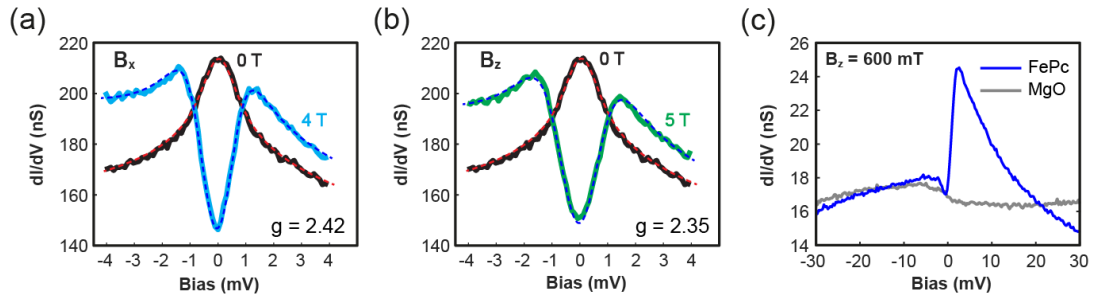

Fig. S1 | (a)(b) dI/dV spectra showing Kondo resonance at zero field (black lines) and splitting in an (a) in-plane field, B_{x} (blue line) and (b) out-of-plane field, B_{z} (green line). The dashed lines are the fits based on the scattering model proposed by Markus Ternes. Tip was positioned at the

center of FePc. (c) dI/dV spectra taken with a spin-polarized tip above the center of FePc and a bare MgO area at B_z = 600 mT. Spectroscopy conditions: (a)(b) Tip was set as V = 4 mV, I_{set} = 700 pA before disabling the feedback and a modulated voltage V_{mod} = 0.1 mV was applied; (c) V = -30 mV, I_{set} = 500 pA, V_{mod} = 1 mV. All dI/dV measurements were performed at the STM temperature of 1.7 K.

2. Extraction of μ_{FePc} by using different methods and in different magnetic fields

According to the equation (2) in the main text, the magnetic moment of FePc (μ_{FePc}) can be extracted by fitting either $f_0 \propto B_{tip}(I)$ or $f_0 \propto B_z$. We thus compared the μ_{FePc} deduced by these two methods. Figure S2(a) shows the ESR spectra measured with varied tunneling current (I_{set}) in a given out-of-pane (B_z) external field. The change of resonance frequency as a function of I_{set} is plotted in Fig. S2(b), yielding μ_{FePc} of 1.008±0.001 μ_B, in good agreement with the g-factors measured in Supplementary Section 1. Figure S2(c)-(d) are results of external field dependence ESR spectra taken at same I_{set}. The fitting gives μ_{FePc} of 0.959±0.010 μ_B. The magnetic moment obtained by varied-current and varied-external field ESR measurements show a deviation of less than 5%. This deviation is likely from the overestimated exchange coupling interaction between the tip and the underneath spin when the tip is infinitely far (i.e. when I_{set} = 0). In this extreme limit, the tip field may deviate from the linear relation with the tunneling current setpoint, leading to a slight deviation in the μ_{FePc} extracted from the varied-current measurements compared to the varied-external field measurements. However, the coupling energy of FePc dimers are not subject to the absolute value of the magnetic moments and within this deviation and we could still utilize the tip field as a control of the local magnetic field.

In addition, we found that the magnetic moment of individual FePc molecules was nearly isotropic in different directions of the external magnetic field. Figures S2(e)-(h) show the ESR measurements performed in in-plane external magnetic field (B_x). We measured a μ_{FePc} of also approximately 1 μ_B, similar to the one obtained in B_z field. The less than 5% deviation between μ^{z}_{FePc} and μ^{x}_{FePc} may stem from the inhomogeneous spin occupied orbital configuration along different directions.

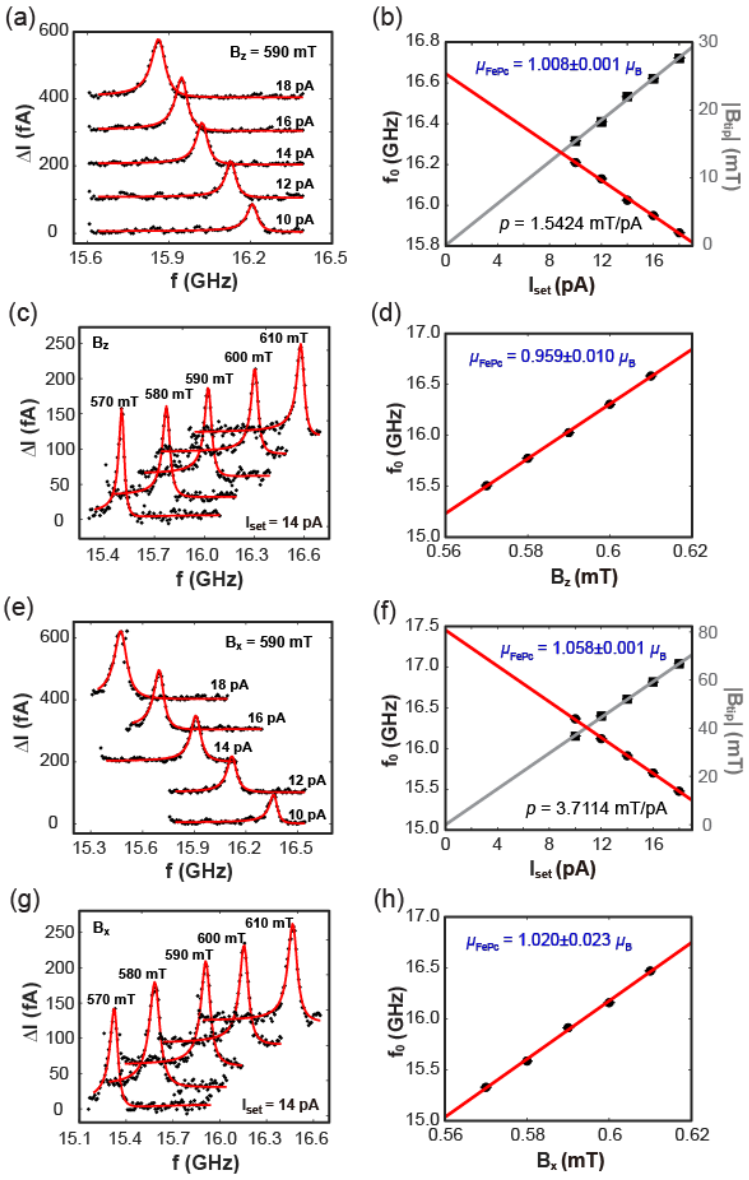

Fig. S2 | (a)(b) Current-dependence ESR spectra measured in out-of-plane field B_z = 590 mT. The linear fit of resonance frequencies as a function of current yields the magnetic moment of FePc which is 1.008±0.001 μ_B. In addition, the corresponding tip field at a given current can be described by a conversion coefficient which is p = 1.5424 mT/pA. (c)(d) External field dependence ESR spectra measured in different out-of-plane fields with the same tunneling current setpoint, showing μ_{FePc} = 0.959±0.010 μ_B. (e)(f) Current-dependence ESR spectra measured in in-plane field B_x = 590 mT, giving the magnetic moment of FePc of 1.058±0.001 μ_B. (g)(h) External field dependence ESR spectra measured in different B_x (in-plane field) with the same tunneling current setpoint, showing μ_{FePc} = 1.020±0.023 μ_B. All ESR measurements were performed with the same spin-polarized tip and on same FePc molecule. ESR conditions: V = 100 mV, V_{rf} = 40 mV.

3. Statistics on magnetic moment of different individual FePc molecules

Figure 1(d) in the main text demonstrates the magnetic moment extracted by tip field dependence ESR measurements in a given B_z field. We then measured ESR on the same FePc

molecule with the same tip in varied B_z fields at a given tip field (same tunneling current). As shown in Fig. S3(a), by fitting f_0 linearly to B_z, we obtained a μ_{FePc} of 0.950±0.048 μ_B, which is very close to the value measured by tip field dependence measurements.

Figure S3(b) plots the magnetic moments of different individual FePc molecules extracted from varied tip field measurements in fixed external magnetic fields, giving an averaged magnetic moment of 1.028±0.023 μ_B.

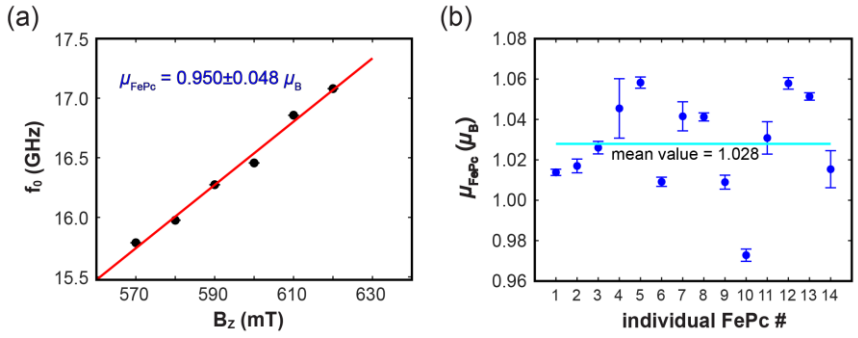

Fig. S3 | (a) Resonance frequency shift as a function of external magnetic field at given tip field (I_{set} = 15 pA) with same tip and on same FePc molecule as measured in Fig. 1(c). ESR conditions: V = 100 mV, V_{rf} = 10 mV. (b) Magnetic moments of 14 individual FePc molecules obtained by tip field dependence ESR measurements in given external magnetic fields.

4. Current-dependence ESR spectra of different FePc-FePc dimers and statistics on coupling energy

In our experiments, we found abundant naturally formed FePc clusters. The majority was FePc-FePc dimer and two favored adsorption configurations were found, namely (3, 4) and (0, 5) by counting the oxygen lattices passing between two Fe centers. The center-center distance for (3, 4) and (0, 5) dimers are exactly the same. Occasionally, we found (2, 5) dimers but much fewer in numbers. In these dimers, each ligand prefers to orient to (2, 1) direction, as illustrated by the black arrows in Fig. S4(a), (d), and (g). Moreover, the two nearest aromatic rings belonging to two molecules are also arranged in (2, 1) configuration (*i.e.* the heads of the two black arrows are apart by 2×1 oxygen atoms). This is consistent with the optimized adsorption configuration of a FePc-FePc dimer by DFT calculations. The relative possibility of finding these dimers is 38%, 53%, 9% for (3, 4), (0, 5), (2, 5), respectively (Fig. S5). The coupling energy is similar when the tip is positioned on any molecule within the dimer. The comparison of current dependence ESR spectra and coupling energy measured on each molecule in the dimers are shown in Fig. S4(b), (c), (e), (f), (h), and (i).

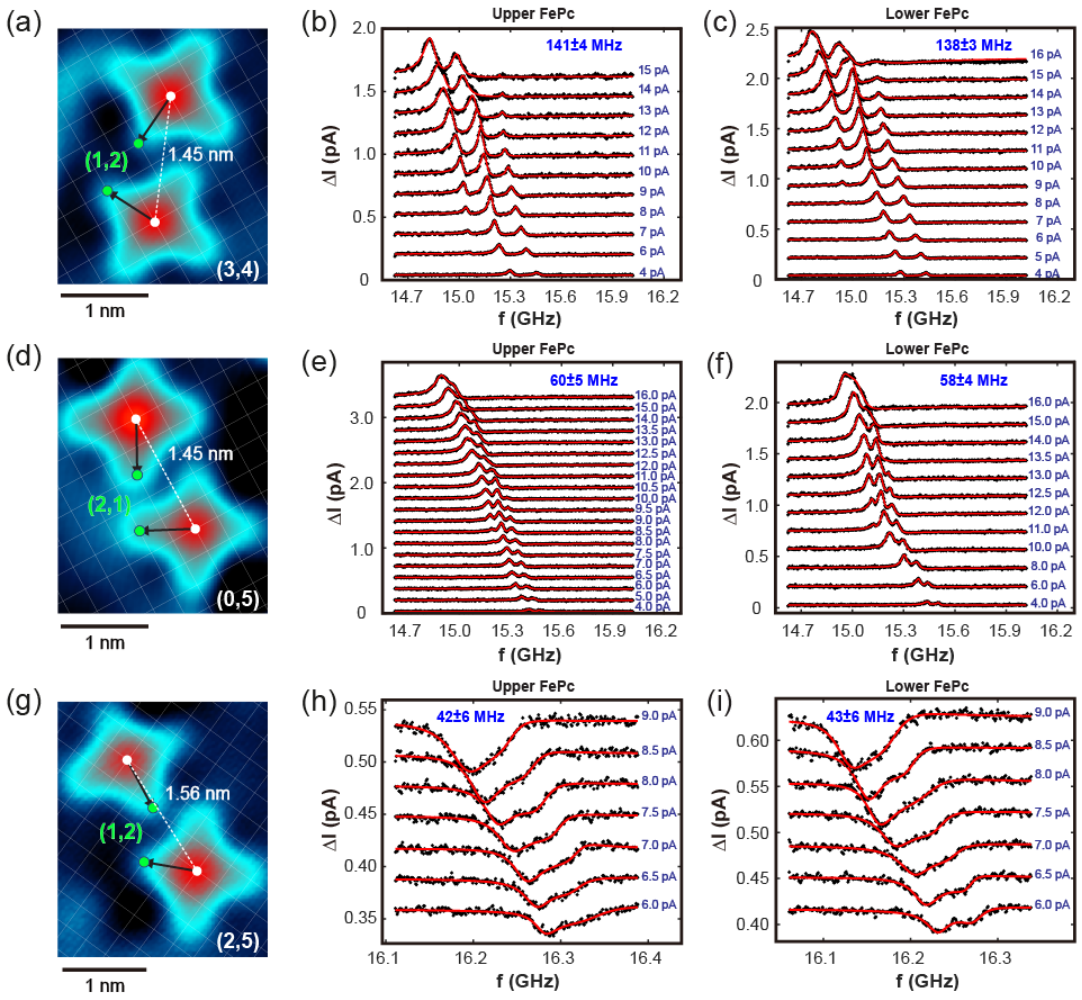

Fig. S4 | (a)(d)(g) STM images of (3, 4), (0, 5), and (2, 5) dimer. Dashed white lines connect two Fe centers. Black arrows (start from the Fe center and end at the oxygen atom underneath the aromatic ring) indicate the relative alignment of molecular ligands. In these dimers, the two nearest aromatic rings belonging to two molecules are apart by 2×1 oxygen lattices, as highlighted by green coordinates. The middle and right columns exhibit current dependence ESR spectra measured on both molecules in a dimer. Coupling energy obtained by measuring ESR splitting is labelled on the top of each panel. Scanning conditions: (a)(d) V = 180 mV, I_{set} = 20 pA; (g) V = 150 mV, I_{set} = 8 pA. ESR conditions: V = 100 mV, (b)(c) V_{rf} = 50 mV, B_z = 550 mT; (e)(f) V_{rf} = 40 mV, B_z = 550 mT; (h)(i) V_{rf} = 25 mV, B_z = 570 mT. The ESR spectra have been vertically shifted one after another by (b) 150 fA; (c) 170 pA; (e)(f) 170 pA; (h)(i) 70 pA for clarity.

By measuring 32 molecules in different dimers, we obtained average coupling energy (J+D) for (3, 4), (0, 5) and (2, 5) dimer of 134±19 MHz, 64±7 MHz, and 42±6 MHz, respectively (Fig. S5). The dipolar contribution D is estimated by considering two point spins with 1 μ_B and has a value of 17 MHz for (3, 4) and (0, 5) dimers and 14 MHz for (2, 5) dimer. As demonstrated in Fig. 3, the change in coupling energy for different dimer configurations is a result of different ligand-ligand distance. In addition, the less occurrence of (3, 4) configuration than (0, 5) configuration may imply the subtle difference between these two configurations which are caused by different adsorption energy, although it is difficult to distinguish from the topography image.

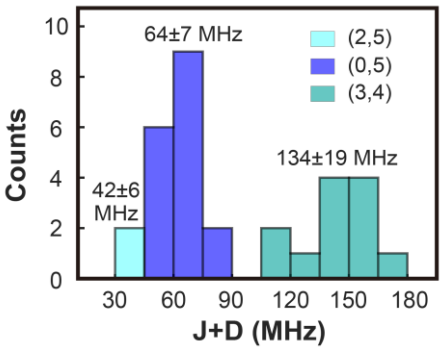

Fig. S5 | Statistics of FePc-FePc dimer configurations and corresponding ESR splitting. In all these measurements, only an out-of-plane field was applied.

5. ESR transitions in Heisenberg two-spin system with the tip field detuning effect

In our experiment, the Zeeman energy (~16 GHz) set by external magnetic field is much stronger than the intermolecular coupling energy (~100 MHz). This implies that FePc spins are aligned to the direction of the external field. Thus, we can solve the Hamiltonian in equation (3) by using Zeeman basis $|00\rangle, |01\rangle, |10\rangle$, and $|11\rangle$. $|0\rangle$ and $|1\rangle$ are eigenvectors of spin operator $\boldsymbol{S}$ along the external field direction of first and second spin, respectively. Due to the existence of inter-spin coupling, two of the eigenstates, represented as $|-\rangle$ and $|+\rangle$, become a linear superposition of states $|01\rangle$ and $|10\rangle$, as shown below while $|00\rangle$ and $|11\rangle$ remain the other two eigenstates of Hamiltonian in equation (3):

$$|-\rangle = -\frac{\alpha}{\sqrt{\alpha^2+1}}|01\rangle + \frac{1}{\sqrt{\alpha^2+1}}|10\rangle,$$
$$|+\rangle = \frac{1}{\sqrt{\alpha^2+1}}|01\rangle + \frac{\alpha}{\sqrt{\alpha^2+1}}|10\rangle$$

where α indicates the relative weight of $|01\rangle$, $|10\rangle$ components in the $|-\rangle$ and $|+\rangle$ states, $\alpha = \frac{2(\mu_1-\mu_2)B_{ex}+2\mu_1 B_{tip}+\sqrt{[J-\frac{D}{2}(1-3\cos^2\theta)]^2+[2(\mu_1-\mu_2)B_{ex}+2\mu_1 B_{tip}]^2}}{J-\frac{D}{2}(1-3\cos^2\theta)}$.

The eigenenergies for $|00\rangle$, $|-\rangle$, $|+\rangle$ and $|11\rangle$ are:

$$E_{00} = \frac{1}{4}h[J + D(1-3\cos^2\theta)] - \left(\mu_1 B_{\text{ex}} + \mu_1 B_{\text{tip}} + \mu_2 B_{\text{ex}}\right)$$

$$E_{-} = -\frac{1}{4}h[J + D(1-3\cos^2\theta)] - \frac{1}{2}\sqrt{h^2\left(J - \frac{1}{2}D(1-3\cos^2\theta)\right)^2 + 4\left(\mu_1 B_{\text{ex}} + \mu_1 B_{\text{tip}} - \mu_2 B_{\text{ex}}\right)^2}$$

$$E_{+} = -\frac{1}{4}h[J + D(1-3\cos^2\theta)] + \frac{1}{2}\sqrt{h^2\left(J - \frac{1}{2}D(1-3\cos^2\theta)\right)^2 + 4\left(\mu_1 B_{ex} + \mu_1 B_{tip} - \mu_2 B_{ex}\right)^2}$$

$$E_{11} = \frac{1}{4}h[J + D(1-3\cos^2\theta)] + \left(\mu_1 B_{\text{ex}} + \mu_1 B_{\text{tip}} + \mu_2 B_{\text{ex}}\right)$$

Since we have assumed the first spin is the one under the tip, ESR transition is only allowed when the quantum number m_s of this spin is changed by $\Delta m_s = \pm 1$. Therefore, possible ESR transitions are $|00\rangle \rightarrow |-\rangle$, $|+\rangle \rightarrow |11\rangle$, $|00\rangle \rightarrow |+\rangle$ and $|-\rangle \rightarrow |11\rangle$.

Corresponding frequencies of these transitions are given by:

$$f_1 = \frac{E_- - E_{00}}{h} = -\frac{1}{2}[J + D(1 - 3\cos^2\theta)] + \frac{1}{h}(\mu_1 B_{ex} + \mu_1 B_{tip} + \mu_2 B_{ex}) - \frac{1}{2}\sqrt{\left(J - \frac{1}{2}D(1 - 3\cos^2\theta)\right)^2 + \frac{4}{h}(\mu_1 B_{ex} + \mu_1 B_{tip} - \mu_2 B_{ex})^2}$$

$$f_2 = \frac{E_{11} - E_+}{h} = \frac{1}{2}[J + D(1 - 3\cos^2\theta)] + \frac{1}{4\pi}(\mu_1 B_{ex} + \mu_1 B_{tip} + \mu_2 B_{ex}) - \frac{1}{2}\sqrt{\left(J - \frac{1}{2}D(1 - 3\cos^2\theta)\right)^2 + \frac{4}{h}(\mu_1 B_{ex} + \mu_1 B_{tip} - \mu_2 B_{ex})^2}$$

$$f_3 = \frac{E_+ - E_{00}}{h} = -\frac{1}{2}[J + D(1 - 3\cos^2\theta)] + \frac{1}{h}(\mu_1 B_{ex} + \mu_1 B_{tip} + \mu_2 B_{ex}) + \frac{1}{2}\sqrt{\left(J - \frac{1}{2}D(1 - 3\cos^2\theta)\right)^2 + \frac{4}{h}(\mu_1 B_{ex} + \mu_1 B_{tip} - \mu_2 B_{ex})^2}$$

$$f_4 = \frac{E_{11} - E_-}{h} = \frac{1}{2}[J + D(1 - 3\cos^2\theta)] + \frac{1}{h}(\mu_1 B_{ex} + \mu_1 B_{tip} + \mu_2 B_{ex}) + \frac{1}{2}\sqrt{\left(J - \frac{1}{2}D(1 - 3\cos^2\theta)\right)^2 + \frac{4}{h}(\mu_1 B_{ex} + \mu_1 B_{tip} - \mu_2 B_{ex})^2}.$$

We note that α depends on δ, meaning the dominant ESR transitions vary at different tip fields. Since the tip field direction in our work is always opposite to the external field, B_{tip} naturally contains a negative sign with respect to B_{ex}. In the weak tip field regime, i.e. $B_{tip} \approx 0$, yielding $\delta > 0$ and $\alpha > 1$. Hence, $|01\rangle$ and $|10\rangle$ are the dominant components of $|-\rangle$ and $|+\rangle$ states, respectively, leading to prevailed f_3 (from E_{00} to E_+) and f_4 (from E_- to E_{11}). In comparison, when the tip field is strong, i.e. $B_{tip} \ll 0$, it yields $\delta < 0$ and $\alpha < 1$ which means $|-\rangle$ and $|+\rangle$ state have more weight on $|10\rangle$ and $|01\rangle$, respectively. As a result, f_1 (from E_{00} to E_-) and f_2 (from E_+ to E_{11}) are more prominent while the other two transitions are almost vanishing. When B_{tip} cancels the difference of Zeeman energy of two FePc spins (meaning $\delta = 0$, $\alpha = 1$), $|10\rangle$ and $|01\rangle$ are equally weighted in $|-\rangle$ and $|+\rangle$, f_1 and f_4 have the same intensity and f_2, f_3 merge to one peak (when dipolar coupling contribution is much smaller than exchange coupling contribution), as indicated by the white arrows in Fig. 2(c) and 2(f).

In the strong tip field regime of both FePc dimers, we found that the ESR signal at f_1 driving the transition from $|00\rangle$ to $|10\rangle$ appears at lower frequency than the one at f_2 driving the transition from $|01\rangle$ to $|11\rangle$. This implies that the $|10\rangle$ state is energetically favorable compared to the $|11\rangle$ state. In addition, the fitted J value based on the model Hamiltonian gives a positive number. These results indicate that the exchange interaction of the two FePc molecules prefers to be antiferromagnetically (AFM) coupled for both (3, 4) and (0, 5) dimers.

For a given two-spin system where μ_1, μ_2, B_{ex}, J, D, and θ are known, the energy of

each state can be plotted as a function of B_{tip}, as shown in Fig. S6(a). Here, we used the approximate experimental values for each parameter: $\mu_1 = 1.02\ \mu_B$, $\mu_2 = 0.98\ \mu_B$, $B_{ex} =$ 550 mT, $J =$ 150 MHz, $D =$ 15 MHz, θ is 90° (meaning with an out-of-plane field only). As illustrated by Fig. 1, the tip field in our case had an opposite direction compared to external magnetic field, so B_{tip} was set to vary from -60 mT to 0. Figure S6(b) presents the four ESR transitions derivated from Fig. S6(a). Taking the thermal population of each state into account (*i.e.* at a STM temperature of T = 1.7 K) and with a reasonable linewidth $\Gamma =$ 30 MHz, we were able to simulate the ESR signal in frequency sweep at different tip fields, as shown in Fig. S6(c).

Moreover, fitting the experimentally measured f_1, f_2, f_3 and f_4 (Fig. 2(c) and (f)) as a function of tip field based on above equations (the overlapped dashed curves in Fig. 2(c) and (f)) allow us to determine the magnetic moment of each molecule and the exchange and dipolar coupling energy. For the (3, 4) dimer shown in Fig. 2(a), we obtained μ_1 = 1.006 μ_B, μ_2 = 0.983 μ_B, J = 135 MHz, D = 15 MHz; for the (0, 5) dimer shown in Fig. 2(d), we obtained μ_1 = 1.011 μ_B, μ_2 = 0.991 μ_B, J = 54 MHz, D = 10 MHz.

Notably, when B_{tip} cancels the difference of Zeeman energy of two FePc spins (*i.e.* $\delta = 2\mu_1 B_{ex} + 2\mu_1 B_{tip} - 2\mu_2 B_{ex} = 0$, α = 1), $|10\rangle$ and $|01\rangle$ are equally weighted in states $|-\rangle$ and $|+\rangle$ and the difference between f_2 and f_3 becomes: $f_3 - f_2 = -\frac{3}{2}D(1 - 3\cos^2\theta)$. This means f_1 and f_4 have the same intensity and f_2, f_3 merge into one peak when the dipolar coupling contribution D becomes negligible. To extract the coupling strength of a two-spin system in a simpler way, we can read the ESR splitting Δf between f_1 and f_2, f_3 and f_4:

$$\Delta f = f_2 - f_1 = f_4 - f_3 = J + D(1 - 3\cos^2\theta),$$

which is independent of the tip field. Thus, we can extract the exchange and dipolar coupling constant J and D simply by fitting the ESR splitting as a function of external field direction with respect to the sample plane (Fig. 3(b)).

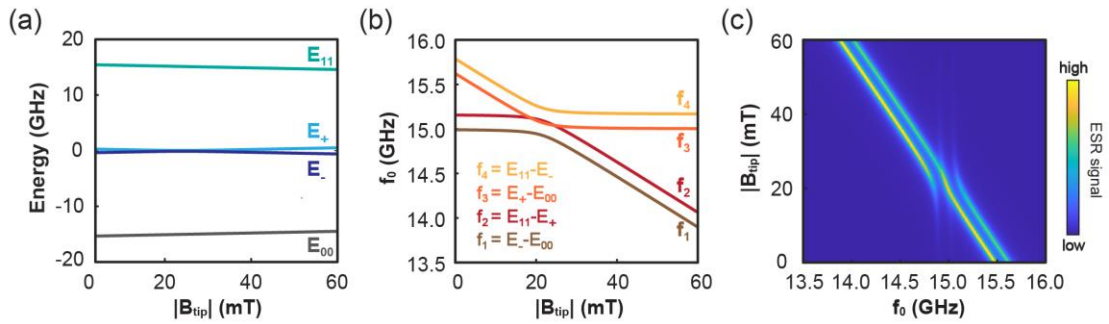

Fig. S6 | (a) Modelled energy levels of the four spin states in a dimer as a function of tip field. (b) Corresponding frequencies of four possible ESR transitions which is calculated from energy levels shown in (a). (c) Simulated ESR spectra as a function of tip field plotted in color scale. Model parameters were selected as: $\mu_1 =$ 1.02 μ_B, $\mu_1 =$ 0.98 μ_B, $B_{ex} = B_z =$ 550 mT, $B_{tip} =$ -60~0 mT, T = 1.7 K, J = 150 MHz, D = 15 MHz, ESR linewidth $\Gamma =$ 30 MHz.

6. FePc-FePc dimers with closer ligand-ligand distance

In addition to the dominant FePc dimer configuration, of which two nearest lobes are arranged in (2, 1) (like those shown in Fig. S4), we also found dimers having closer ligand-ligand distance, as shown in Fig. S7. The (5, 1) dimer in Fig. S7(a) has a center-center distance of 1.48 nm, slightly larger than the (0, 5) dimer, 1.45 nm. However, the two nearest lobes are arranged in (2, 0) configuration and thus has closer ligand-ligand distance than the (0, 5) dimer with (2, 1) lobe-lobe configuration (Fig. S4(d)). This gives rise to an enhanced coupling strength, 105 MHz, of the (5, 1) dimer (Fig. S4(b)) compared to an averaged coupling energy, 64 MHz, of the (0, 5) dimer (Fig. S5).

Figure S7(c) and (e) display two (5, 3) dimers of same center-center distance (1.69 nm) but very different lobe-lobe configuration, (0, 2) and (1, 1), respectively. For the (5, 3) dimer with (0, 2) lobe-lobe configuration, the center-center distance is too far to generate a measureable coupling interaction between two molecules with our ESR linewidth of about 30 MHz under these conditions. Reflected in the ESR spectrum, only a single peak can be resolved (Fig. S7(d)). In contrast, when the two molecules are arranged in a much closer (1, 1) lobe-lobe configuration (Fig. S7(e)), the intermolecular coupling is prominently enhanced to 145 MHz (Fig. S7(f)). The measurements of these specific FePc dimers with closer ligand-ligand distance strongly indicate that the spin distribution on molecular ligands influences spin-spin interaction. However, these kind of dimers were rarely found likely due to the stronger repulsive force by the peripheral hydrogen atoms when two lobes are closer to each other.

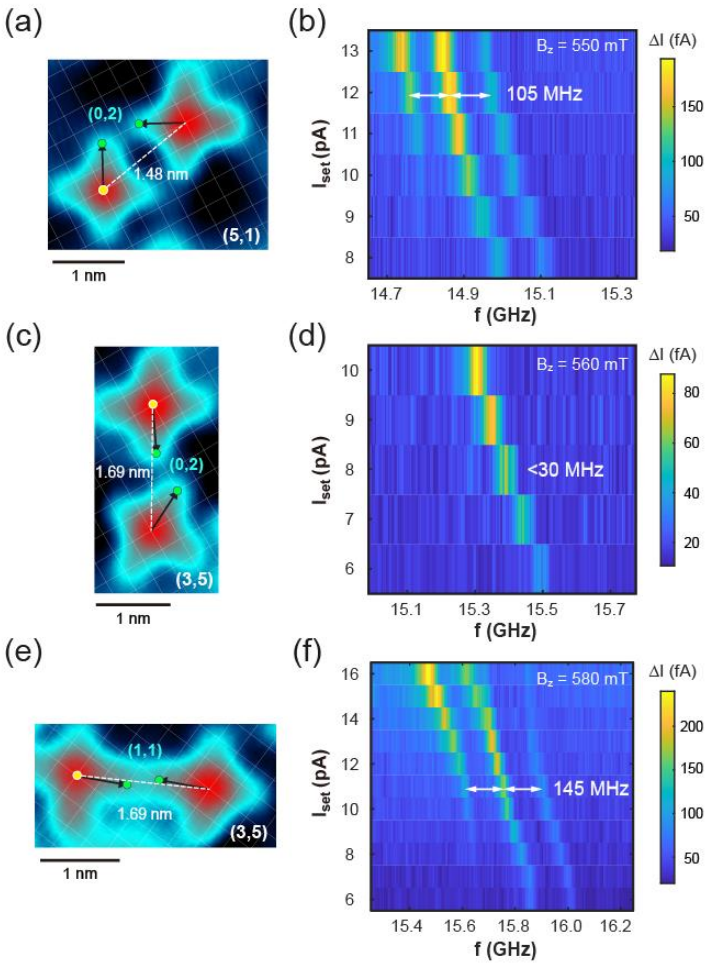

Fig. S7 | (a) STM images of a (5, 1) dimer with (0, 2) lobe-lobe configuration and (c)(e) two (5, 3) dimers with (0, 2) and (1, 1) lobe-lobe configuration, respectively. (b)(d)(f) Corresponding current dependence ESR spectra plotted in color scale. The coupling energy for each dimer is 105±2 MHz, <30 MHz and 145±6 MHz, respectively. The tip was positioned on the yellow spots marked in STM images. Only out-of-plane field was applied during ESR measurements. Scanning conditions: (a)(c) V = 200 mV, I_{set} = 20 pA; (c) V = 150 mV, I_{set} = 8 pA. ESR conditions: V = 100 mV, (b) V_{rf} = 35 mV; (d) V_{rf} = 20 mV; (f) V_{rf} = 36 mV.

7. Fitting of J as a function of Ti_B-Fe distance and Ti_B-ligand distance

By measuring 14 FePc-TiB pairs, we observed clear decay of J as both Fe center-Ti_B distance (r) and ligand-Ti_B distance (l) increases, as shown in Fig. S8(a) and (b). Fe center in the molecule is denoted as (0, 0)) and l is the lateral distance between Ti_B atom and the ligand center. By assuming l and r are two irrelevant variables and the coupling energy J varies exponentially as a function of both r and l, we use the following equation to fit the experimental data (J_0 is set as 1 MH to unify the unit and simplify the fit):

$$J(r,l) = J_0(c_1 \cdot e^{-r/\lambda} + c_2 \cdot e^{-l/\lambda}).$$

The (1.42, 0.71) site was chosen as a center of ligand after trying with a series of different lattice sites along the (2, 1) direction in the fit and comparing the ratio of c_1 and c_2 with spin distribution on center (90%) and ligand (10%) and center suggested by DFT results, as shown in Figs. S8(c)-(e).

Thus, the relation between l and the center-center distance r, the angle between ligand axis and connection of Ti_B-Fe (φ) is $l = \sqrt{(r\sin\varphi)^2 + \left(r\cos\varphi - \sqrt{(0.71)^2 + 1.42^2}\cdot 0.29\right)^2}$.

Here, the coupling between Ti_B and the second nearest ligand is ignored due to the much larger distance. The fitting parameters are obtained as $c_1 = 2.63\times10^{10}$, $c_2 = 8.25\times10^{8}$, $\lambda =$ 0.0506 nm (Fig. S8(c)-(f)) and can reproduce the experimental results with great precision (Fig. S8(g)). Figure S8(h) manifests clearly the two-dimensional decay of J with increasing r and l.

Since J can be written also as

$$J(r,\varphi) = J_0(c_1 \cdot e^{-r/\lambda} + c_2 \cdot e^{-\sqrt{(r\sin\varphi)^2+\left(r\cos\varphi-\sqrt{(0.71)^2+1.42^2}\cdot 0.29\right)^2}/\lambda}),$$

by varying φ from 0 to π/4 and applying reflection and rotation manipulation according to molecular axes, we can simulate the spatial evolution of J with the nearby atom spin occupying different sites around the molecule. The simulated spatial energy map (colored contours in Fig. 5) agrees well with the experimental data (colored dots in Fig. 5), showing an energy valley along the 45° molecular symmetry axis where l is maximized with the same r.

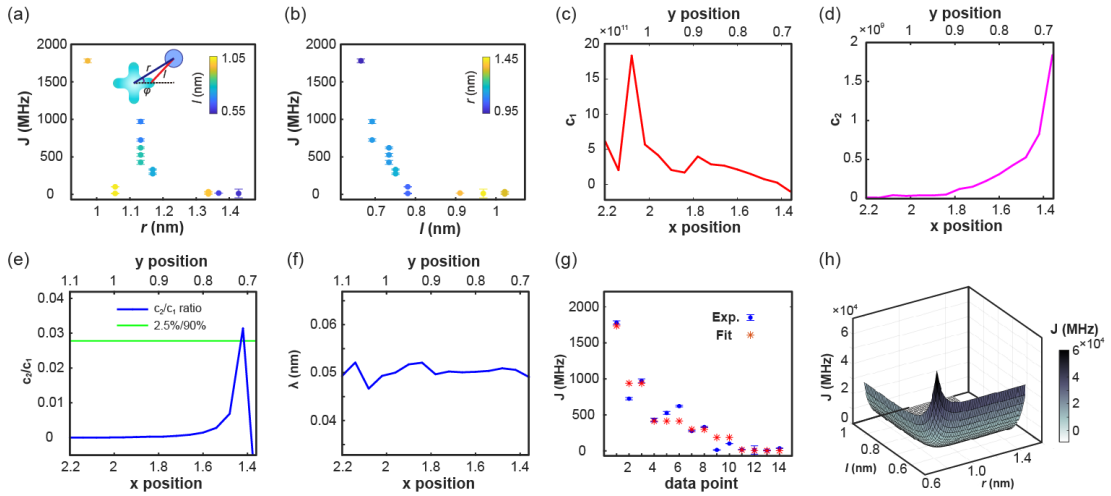

Fig. S8 | (a) Exchange coupling energy (J) as a function of Fe-Ti$_B$ distance r. Pairs with different Ti$_B$-ligand distance l (from Ti$_B$ to the (1.42, 0.71) lattice site) are distinguished in color scale. Inset: definition of r, l and φ. φ is the angle between the connection of Fe-Ti$_B$ and molecular axes. (b) J as a function of l. Corresponding r of each data point is expressed in color scale. (c)(d) Fitted c_1 and c_2 as a function of different lattice sites. (e)(f) Fitting parameters as a function of different lattice sites. (g) Comparison between experimentally measured J of 14 FePc-Ti$_B$ pairs and fitted J by using two-variable exponent function. (h) Simulated two-dimensional decay of J as a function of r and l.

8. Details of DFT calculations

All density functional theory (DFT) calculations were performed using Quantum Espresso (version 6.5) which implements DFT using plane waves and pseudopotentials[35,36]. Pseudopotentials were chosen based on the SSSP library and the basis set was expanded using a kinetic cutoff of 40 Rydberg[37]. All pseudopotentials use the generalized gradient approximation of Perdew, Burke, and Ernzerhof (PBE) and we treat van der Waals interaction using Grimme's D3[38,39].

We first confirmed that DFT accurately reproduces the experimentally found S = 1/2 of FePc on MgO/Ag(100) surface. The system is modelled as 4 monolayers (ML) of silver capped by 2 ML of MgO exposing the (100) surface. Details about the setup and convergence of the MgO/Ag(100) system can be found in Ref. 42. The structure is expanded into a lateral supercell of 2×2 nm^2 which separates the FePc molecule by more than 6 Å from its periodic images. In the z-direction, the cell is padded with 12 Å of vacuum. Our calculations indicate that the relaxed configuration with a (2, 1) lobe orientation is indeed the lowest energy configuration and the Fe sits 2.7 Å above the oxygen (Fig. S9(b)). An analysis of the local density of states (LDOS) (Fig. S9(a)) confirms that the FePc is negatively charged (*i.e.* FePc^{1-}) with respect to its neutral electronic configuration in vacuum and adopts an electronic configuration $(a_{1u})^2$ $(e_g)^4$ $(b_{2g})^2$ $(a_{1g})^1$ with one unpaired excess electron in a dz^2 type orbital. Further analysis of the frontier orbital indicates that it consists of 90% dz^2 and 10% contributions from the ligands. This sharp charge transition is characteristic for molecules decoupled from a metal support by insulating layers[43]. In comparison, while the spin density spreads significantly along the

molecular ligands (Fig. S10(a)), the spin-1/2 hydrogenated titanium atom adsorbed on O-O bridge site (Ti_B) has very compact spin density around the atom center (Fig. S10(b)). Therefore, a Ti_B atom can be considered as a point magnet.

Furthermore, we confirmed that charging the cell with an excess electron and removing the silver gives an identical $FePc^{1-}$ configuration on the molecule. Therefore, we were able to remove the silver in subsequent calculations which gives a considerable speedup.

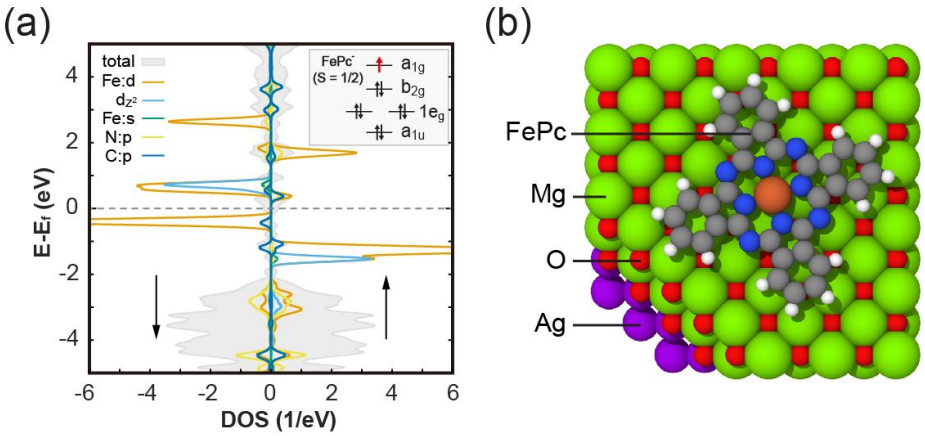

Fig. S9 | (a) Local DOS of the FePc molecule on MgO/Ag(100) highlighting the unpaired dz^2 orbital. Inset: electron occupancy of molecular frontier orbitals. (b) Computational setup of an individual FePc on MgO surface atop an Ag(100) substrate.

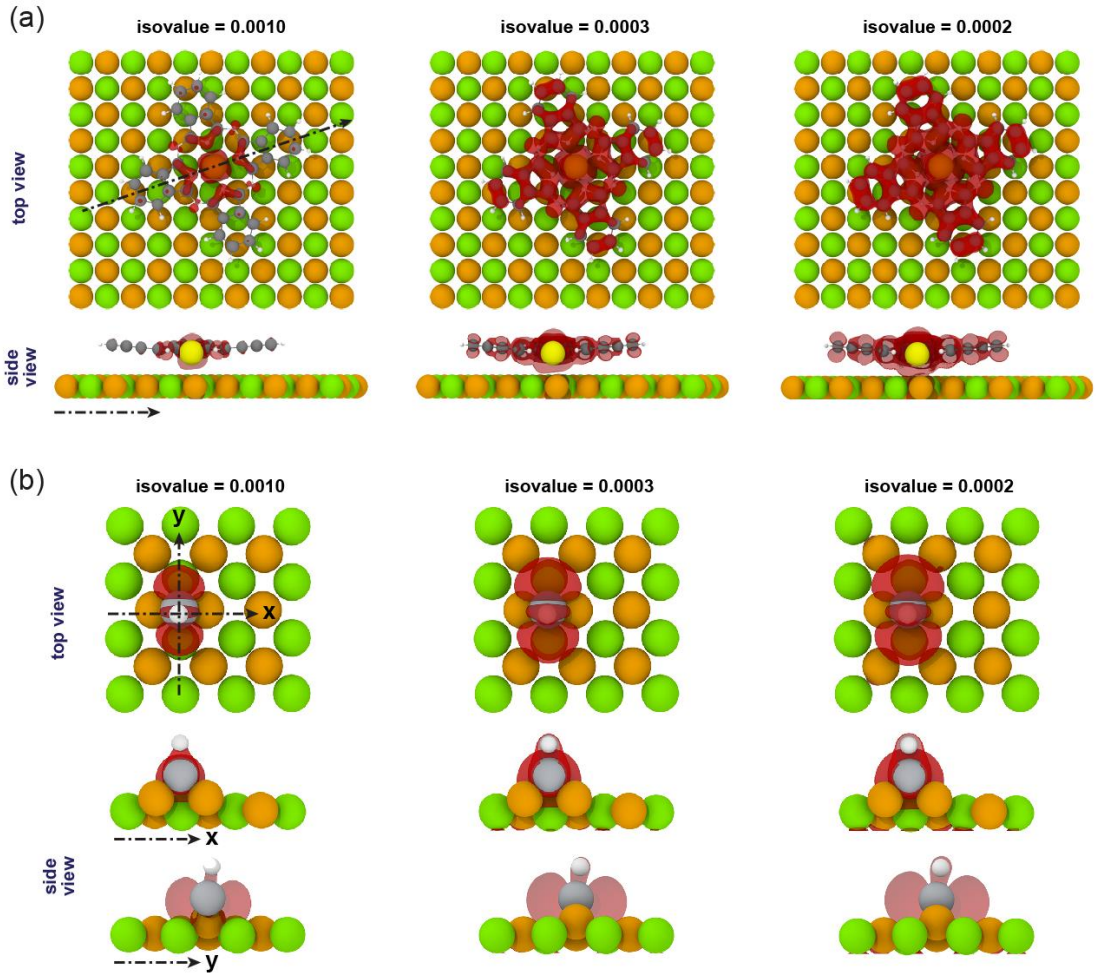

Fig. S10 | Spin density isosurface plot of (a) a FePc molecule and (b) a Ti_B atom on MgO surface with different isovalues. (a) indicates the spin density distributed on both FePc center and outer ligands while in (b) the spin density of a Ti_B atom is highly localized. Upper panel: top view. Lower panel: side view cleaved along the dashed lines.

In the FePc-FePc dimer case, to accommodate both molecules, the cell is laterally expanded to make sure that the separation of dimers and their periodic image is at least 5 times larger than the inter-dimer distance. This is based on the assumption that the dimer interaction is dominated by static exchange that decays exponentially in vacuum. Convergence tests with larger cells indicate that this separation is sufficient to remove spurious effects due to periodic boundary conditions. Due to the single-determinant nature of the Kohn-Sham (KS) auxiliary wave-functions used in DFT, we don't have direct access to the singlet/triplet basis and rely on the broken-symmetry approach introduced by Noodleman[30]. In brief, this approach maps the KS energies of the high-spin ($m_s = 1$) and the broken symmetry ($m_s = 0$) state to the diagonal elements of the Heisenberg Hamiltonian. This method has known limitations, however, they have also been shown to give reliable results in the limiting case of two spin-1/2 centers with vanishing overlap of orbitals (*i.e.* the case of fully localized electrons at long distances), but is known to likely give unphysical results when the two spin centers are located on the same molecular units, *e.g.* in the case of biradicals[44,45].

To investigate the difference in exchange coupling for all observed dimer configuration, we

calculated the energy difference between the high spin (corresponding to FM coupling) and broken symmetry (AFM coupling) configuration for a set of geometries where one FePc molecule is slightly rotated around its Fe center whilst the other is kept fixed (Fig. S11(a)). This does not change the Fe-Fe distance but changes the ligand-ligand distance as shown in Fig. S11(b). We then calculated the exchange coupling strength when the molecule is rotated by an angle of ϕ (Fig. S11(c)). When the energy difference is plotted as a function of the minimum ligand-ligand distance (d_{min}), a clear exponential dependence is found (Fig. S11(d)). This is a strong indicator that the dominant mechanism here is exchange mediated by the ligands which contribute around 10% to the frontier orbital as discussed earlier. The subtle difference in ligand-ligand distance for each observed dimer configuration then explains the difference in observed exchange coupling strength. Focusing on the (3, 4) and (0, 5) configurations as shown in Fig. S11(d), we find that in both cases the interaction energy decays exponentially $\sim\exp(-d_{\mathrm{min}}/\lambda)$ with a characteristic length of $\lambda = 0.0345$ nm, a value very similar to previous calculations of the exchange interaction decay length for nickelocene[31]. We note that the dacay of the exchange interaction in a molecular dimer on MgO surface is lower than in vacuum ($\lambda \sim$ 0.044 nm), indicating a screening effect of the MgO layers.

Using the computationally optimized (also experimentally observed) (2, 1) lobe configuration for the (3, 4), (0, 5) and (2, 5) dimer arrangements, DFT calculation gives exchange coupling strengths in good agreement with the experimental value (Fig. S11(e), same as Fig. 3(d)). We note that based on previous studies, this agreement in the μeV (MHz) energy range is somewhat coincidental, as differences up to a factor of 5 in the exchange energy can be routinely observed when changing the exchange-correlation functional[46]. Whilst the absolute values might therefore be subject to cancellation of errors in the calculation, the trends observed between different dimer configurations should be reliable and are in line with experimental results.

In conclusion, the difference in observed exchange energy for different dimer configurations can be explained sufficiently well by their minimum ligand-ligand distance indicating that the exchange measured at the molecule center is mediated by the tails of the wave-function on the ligands.

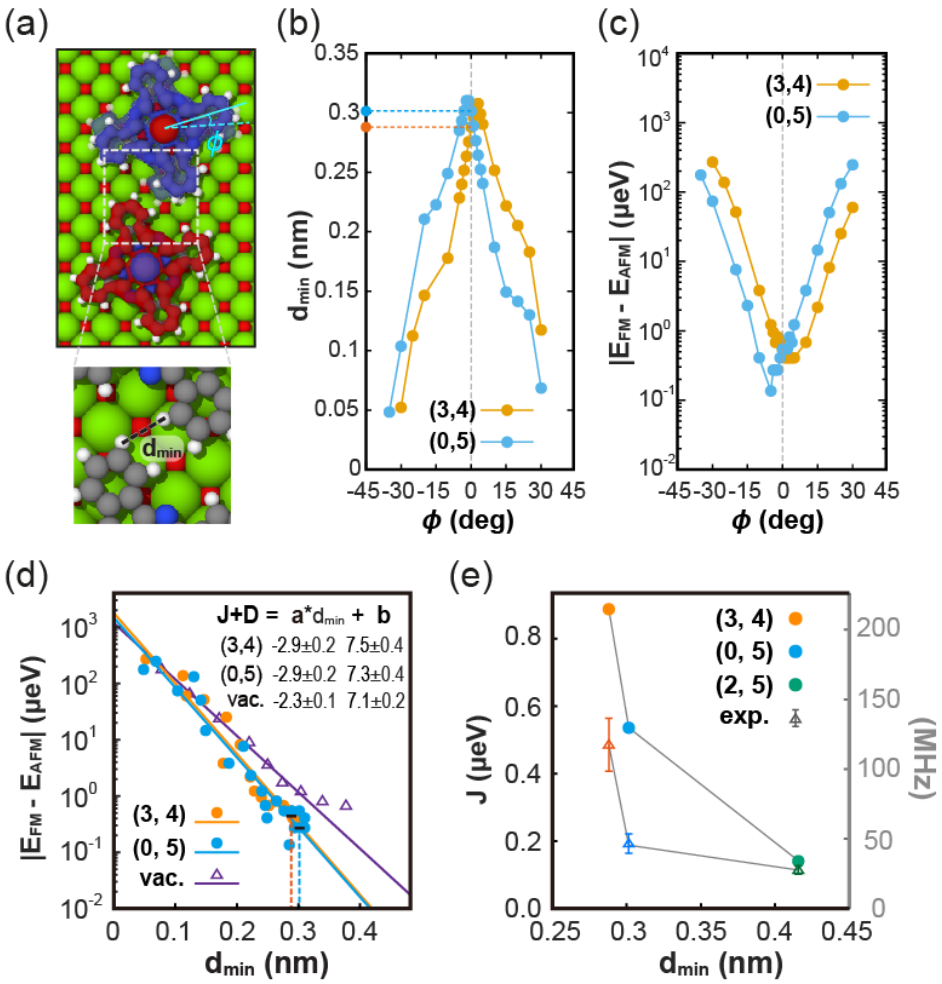

Fig. S11 | (a) Upper panel: AFM coupled (m_s = 0) FePc-FePc dimer in (3, 4) configuration on MgO. During calculation, the upper FePc is rotated concentrically by an angle of ϕ while the lower one is fixed. The spin-polarziation isosurface is shown here (red: positive, blue: negative). Lower panel: definition of our minimal ligand-ligand distance (d_{min}) metric used to calculate the decay of exchange energy. (b) Variation of d_{min} as a function of ϕ. (c)(d) Calculated energy difference between FM and AFM coupling as function of ϕ and d_{min}, respectively, for (3, 4) and (0, 5) configuration. The case for a dimer in vacuum (shorted as vac.) is shown for reference in (d). (e) Comparison of calculated and experimentally measured exchange coupling energy of different dimer arrangements. The experimentally measured exchange coupling energies were obtained by subtracting the dipolar contribution (considering two point spins with 1 μ_B) from the ESR splitting (17 MHz for (3, 4) and (0, 5) dimers and 14 MHz for (2, 5) dimer). (c) is the same plot as Fig. 3(d) in the main text but in linear scale.

References

[30] Noodleman, L. Valence bond description of antiferromagnetic coupling in transition metal dimers. *J. Chem. Phys.* **74,** 5737–5743 (1981).

[31] Czap, G. et al. Probing and imaging spin interactions with a magnetic single-molecule sensor. *Science* **364,** 670–673 (2019).

[35] Giannozzi, P. et al. QUANTUM ESPRESSO: a modular and open-source software project for

quantum simulations of materials. *J. Phys. Condens. Matter* **21,** 395502 (2009).
[36] Giannozzi, P. et al. Advanced capabilities for materials modelling with Quantum ESPRESSO. *J. Phys. Condens. Matter* **29,** 465901 (2017).
[37] Prandini, G., Marrazzo, A., Castelli, I. E., Mounet, N. & Marzari, N. Precision and efficiency in solid-state pseudopotential calculations. *npj Comput. Mater.* **4,** 1–17 (2018).
[38] Perdew, J. P., Burke, K. & Ernzerhof, M. Generalized gradient approximation made simple. *Phys. Rev. Lett.* **77,** 3865–3868 (1996).
[39] Grimme, S., Hansen, A., Brandenburg, J. G. & Bannwarth, C. Dispersion-corrected mean-field electronic structure methods. *Chem. Rev.* **116,** 5105–5154 (2016).
[40] Ternes, M. Spin excitations and correlations in scanning tunneling spectroscopy. *New J. Phys.* **17,** 063016 (2015).
[41] The experimental data was fit by using the program-scripts developed by Markus Ternes.
[42] Wolf, C., Delgado, F., Reina, J. & Lorente, N. Efficient ab Initio multiplet calculations for magnetic adatoms on MgO. *J. Phys. Chem. A* **124,** 2318–2327 (2020).
[43] Hollerer, M. et al. Charge transfer and orbital level alignment at inorganic/organic interfaces: the role of dielectric interlayers. *ACS Nano* **11,** 6252–6260 (2017).
[44] Malrieu, J. P., Caballol, R., Calzado, C. J., De Graaf, C. & Guihéry, N. Magnetic interactions in molecules and highly correlated materials: physical content, analytical derivation, and rigorous extraction of magnetic hamiltonians. *Chem. Rev.* **114,** 429–492 (2014).
[45] Ferré, N., Guihéry, N. & Malrieu, J. P. Spin decontamination of broken-symmetry density functional theory calculations: Deeper insight and new formulations. *Phys. Chem. Chem. Phys.* **17,** 14375–14382 (2015).
[46] Sheng, X., Thompson, L. M. & Hratchian, H. P. Assessing the calculation of exchange coupling constants and spin crossover gaps using the approximate projection model to improve density functional calculations. *J. Chem. Theory. Comp.* **16,** 154–163 (2020).